IOP Publishing | International Atomic Energy Agency Nuclear Fusion

Nucl. Fusion **56** (2016) 036023 (14pp) doi:10.1088/0029-5515/56/3/036023

Modeling and control of plasma rotation for NSTX using neoclassical toroidal viscosity and neutral beam injection

I.R. Goumiri[1], C.W. Rowley[1], S.A. Sabbagh[2], D.A. Gates[3], S.P. Gerhardt[3], M.D. Boyer[3], R. Andre[3], E. Kolemen[3] and K. Taira[4]

[1] Department of Mechanical and Aerospace Engineering, Princeton University, Princeton, NJ 08544, USA
[2] Department of Applied Physics and Applied Mathematics, Columbia University, New York, NY 10027, USA
[3] Princeton Plasma Physics Laboratory, Princeton, NJ 08544, USA
[4] Department of Mechanical Engineering, Florida State University, Tallahassee, FL 32310, USA

E-mail: igoumiri@princeton.edu

Received 29 September 2015, revised 22 December 2015
Accepted for publication 26 January 2016
Published 19 February 2016

Abstract

A model-based feedback system is presented to control plasma rotation in a magnetically confined toroidal fusion device, to maintain plasma stability for long-pulse operation. This research uses experimental measurements from the National Spherical Torus Experiment (NSTX) and is aimed at controlling plasma rotation using two different types of actuation: momentum from injected neutral beams and neoclassical toroidal viscosity generated by three-dimensional applied magnetic fields. Based on the data-driven model obtained, a feedback controller is designed, and predictive simulations using the TRANSP plasma transport code show that the controller is able to attain desired plasma rotation profiles given practical constraints on the actuators and the available measurements of rotation.

Keywords: magnetic confinement, feedback control, rotation Control, neutral beam injection, neoclassical toroidal viscosity, NSTX

(Some figures may appear in colour only in the online journal)

1. Introduction

Spherical tokamaks such as the National Spherical Torus Experiment (NSTX [1]) are toroidal magnetic fusion devices that have been proven experimentally to realize theoretical expectations of efficient and compact advanced tokamak operation, producing high plasma pressures in relation to the pressure of the magnetic field used to create the plasma equilibrium. In certain circumstances, these high pressures can cause rapidly growing magnetohydrodynamic (MHD) plasma instabilities that can lead to undesirable effects such as reducing the plasma pressure, or even terminating the plasma (disruption). Many of these instabilities are sensitive to the shear, so the rotation profile plays a key role in regulating these instabilities. The goal of the present study is to describe a model-based approach to controlling the rotation profile in spherical tokamaks, and to apply the approach to a predictive model based on experimental data from NSTX.

The effect of the rotation profile on MHD instabilities has been well studied in recent years. For instance, greater stability of tearing modes has been associated with increased rotation shear [2, 3], while rotation profile shapes that lead to stronger kinetic resonances lead to stabilization of kink/ballooning modes and resistive wall modes [4, 5]. Furthermore, rotational shear can affect plasma turbulence and consequently can have an impact on transport processes and the energy confinement performance of tokamak plasmas [6–8]. In present-day pulsed tokamaks, plasma rotation can evolve, through normal heat and momentum transport processes, toward profiles for which certain MHD modes are unstable. Even if these profiles evolve

by chance to a steady-state profile that is stable, transient processes including edge-localized modes (ELMs), internal transport barriers, and different heating mechanisms can alter plasma profiles further and make them less stable, or unstable [9]. In future large fusion-power-producing tokamak operation (e.g. the fusion nuclear science facility, FNSF [10–12]), disruptions caused by macroscopic instabilities can generate electromagnetic forces and heat loads large enough to damage device components, so it is particularly important to avoid such disruptions, for instance through control of the rotation profile.

There is an abundant literature on plasma control such as kinetic profile control (density and temperature) [13, 14], burn control [13–2, 15, 17–19], toroidal current profile control [20–24], safety factor profile control [25–27], direct control of tearing modes [28, 29] and resistive wall modes [9, 30]. Rotation control in tokamaks has been demonstrated using momentum input from injected neutral beams (NBI) as an actuator [31, 32]. A new and unique aspect of the present work is the use of non-axisymmetric (three-dimensional) magnetic fields as another actuator in closed-loop feedback control to supplement the neutral beam actuator. Rotation alteration by non-resonant, three-dimensional magnetic fields allows more precise, continuous control of the plasma rotation alteration than NBI, as the momentum delivered by the latter occurs in significantly large, discrete increments.

The physical process creating the force on the plasma rotation generated by the applied three-dimensional field, termed neoclassical toroidal viscosity (NTV) [33–35], has been used successfully to affect plasma rotation in a pre-programmed manner on NSTX over a wide range of plasma operation, with quantitative agreement of the experimentally generated torque to theory [36]. NTV is caused by non-ambipolar diffusion of plasma ions and electrons caused by the magnetic field components that break the usual toroidal symmetry of tokamak confinement field. As NTV depends on several important plasma parameters including temperature, and the plasma rotation itself, its use in closed-loop feedback leads to weak nonlinearities which must be investigated to ensure successful control. Details of such elements will be shown throughout this work.

The present work defines a model-based algorithm for plasma rotation control based on experimental data from NSTX [1], that measures the rotational (toroidal) momentum transport in the tokamak. More details about how to measure rotation profile in real-time can be found in [36, 37]. Data-driven modeling techniques have been successfully used in the past to model plasma transport dynamics for active control design in fusion reactors [20–22, 38]. A novel contribution of this work is the development of a one-dimensional partial differential equation model that is computationally inexpensive, and may therefore implemented for real-time control. The present simplified model of plasma momentum transport retains the most important elements of the plasma momentum balance, including the effects of NBI and NTV, and reproduces the general features of the plasma rotation evolution measured in experiments.

Once the model is satisfactorily developed, a further step consists of applying a spectral decomposition method, linearizing the equation about an equilibrium and projecting onto a subspace spanned by Bessel functions, in order to obtain an approximate linear model consisting of just 5 ordinary differential equations. The resulting reduced model is then used to design a controller using standard techniques from optimal control. The advantage of using a reduced-order model is that the resulting controller is also low dimensional, so that it is computable in real time, as well as being easier to tune and design.

The paper is organized as follows. Section 2 describes the data-driven model definition with details about the actuators used, model reduction process and comparison to experimental data. Section 3 describes the optimal control method used to track a desired rotation profile, using both NTV and NBI as actuators, and its implementation through numerical simulation. Section 4 presents the results of the designed controller on a more complete rotation model that can be found in TRANSP, a time dependent code developed at Princeton Plasma Physics Laboratory for both prediction and analysis of tokamak experimental data [39, 40]. Conclusions and future work are discussed in section 5.

2. A simplified model of the toroidal momentum balance

2.1. Model definition

Consider the transport of toroidal angular plasma momentum in a tokamak with the assumption of axisymmetry. To facilitate the analysis, an arbitrary flux surface average $\rho \in [0, 1]$ is used, where $\rho = 0$ and 1 denote the center and the boundary of the plasma, respectively.

Using the work of Goldston [41] and Callen [42], the angular velocity of the plasma ω can be described dynamically by the flux surface average $\langle\cdot\rangle$ of the toroidal momentum equation

$$\begin{aligned}\sum_i n_i m_i \langle R^2\rangle \frac{\partial \omega}{\partial t} + \omega\langle R^2\rangle \sum_i m_i \frac{\partial n_i}{\partial t} + \sum_i n_i m_i \omega \frac{\partial \langle R^2\rangle}{\partial t} \\ + \sum_i n_i m_i \langle R^2\rangle \omega \left(\frac{\partial V}{\partial \rho}\right)^{-1} \frac{\partial}{\partial t}\frac{\partial V}{\partial \rho} \\ = \left(\frac{\partial V}{\partial \rho}\right)^{-1} \frac{\partial}{\partial \rho}\left[\frac{\partial V}{\partial \rho}\sum_i n_i m_i \chi_\phi \langle R^2(\nabla\rho)^2\rangle \frac{\partial \omega}{\partial \rho}\right] \\ - \left(\frac{\partial V}{\partial \rho}\right)^{-1} \frac{\partial}{\partial \rho}\left[\frac{\partial V}{\partial \rho}\sum_i n_i m_i \omega \langle R^2(\nabla\rho)^2\rangle \frac{v_\rho}{|\nabla\rho|}\right] \\ - \sum_i n_i m_i \langle R^2\rangle \omega \left(\frac{1}{\tau_{\phi cx}} + \frac{1}{\tau_{c\delta}}\right) + \sum_j T_j. \end{aligned} \quad (1)$$

The left-hand side of the equation above represents the temporal change in the plasma toroidal angular momentum and the right-hand side terms denote respectively the one-dimensional fluid viscous term, pinch term, momentum loss due to charge exchange and field ripple, and the torque inputs (i.e. neutral beam injection and neoclassical toroidal viscosity).

R is a major radial coordinate, $\partial V/\partial\rho$ is the differential flux surface volume, χ_ϕ is the perpendicular (to the equilibrium magnetic field) momentum diffusivity, $\tau_{\phi cx}$ and $\tau_{c\delta}$ are the time scales of the local momentum loss associated with charge-exchange and field ripple, T_j represents the various torques acting on the system, n_i is the particle density and m_i is the particle mass for each particle species, but for simplicity, only the main plasma ion species (deuterium) are considered in the dynamics.

It is assumed that the plasma cross-sectional shape is well controlled by a separate control loop; therefore $\langle R^2\rangle$, $\langle R^2(\nabla\rho)^2\rangle$, and $\partial V/\partial\rho$ are held fixed. Curve-fits from time-averaged values of these functions (4th (figures 1(*a*) and (*c*)), 5th (figures 1(*b*) and (*d*)) order polynomials or cubic spline (figure 2) interpolation depending on which one gives the smoothest fit) from TRANSP analysis of an experimental plasma are used as approximations. Representative data for a plasma discharge (133 367) is shown in figures 1(*a*)–(*c*) respectively. As it can be seen, the temporal fluctuations of these variables are small. Hence taking the time-average values or even the fixed values at an adequately chosen time ($t = 0.65$ s) is considered to be a close approximation.

It is also assumed for simplicity that the time variation of the mass density is small. This is a reasonable approximation, especially towards the edge ($\rho = 1$), as seen in figure 1(*d*). This assumption may later be removed allowing $\sum_i n_i m_i$ to vary in time for more complex time-dependent systems, but for now, it allows the density time derivative term in the left-hand side of equation (1) to be neglected, resulting in a time-invariant system that is more amenable to control design.

Incorporating these observations into equation (1), we obtain a simplified diffusion equation

$$nm\langle R^2\rangle\frac{\partial\omega}{\partial t} = \left(\frac{\partial V}{\partial\rho}\right)^{-1}\frac{\partial}{\partial\rho}\left[\frac{\partial V}{\partial\rho}nm\chi_\phi\langle R^2(\nabla\rho)^2\rangle\frac{\partial\omega}{\partial\rho}\right] + T_{\mathrm{NBI}} + T_{\mathrm{NTV}}, \tag{2}$$

with boundary conditions

$$\left.\frac{\partial\omega}{\partial\rho}\right|_{\rho=0} = 0 \quad \text{and} \quad \omega|_{\rho=1} = 0. \tag{3}$$

Here, T_{NBI} and T_{NTV} represent the torques arising from neutral beam injection (NBI) and neoclassical toroidal viscosity (NTV). Note that for this significant class of high confinement discharges specific to NSTX, the pinch term and the momentum loss due to charge exchange are small [43, 44] and the momentum loss due to field ripple is not required, as NTV is explicitly determined in this calculation. Details of the models for T_{NBI} and T_{NTV} are shown in sections 2.2.1 and 2.2.2. The Dirichlet boundary condition at the plasma edge ($\rho = 1$) is chosen to be consistent with experimental observations.

A few observations can be made about this simplified model: first, equation (2) is parabolic, ensuring the state operator to be negative definite (all eigenvalues are negative); hence the system is stable, which is a desirable feature from a control viewpoint. Second, this approach captures only the momentum balance for rotation control and does not model potential plasma instabilities.

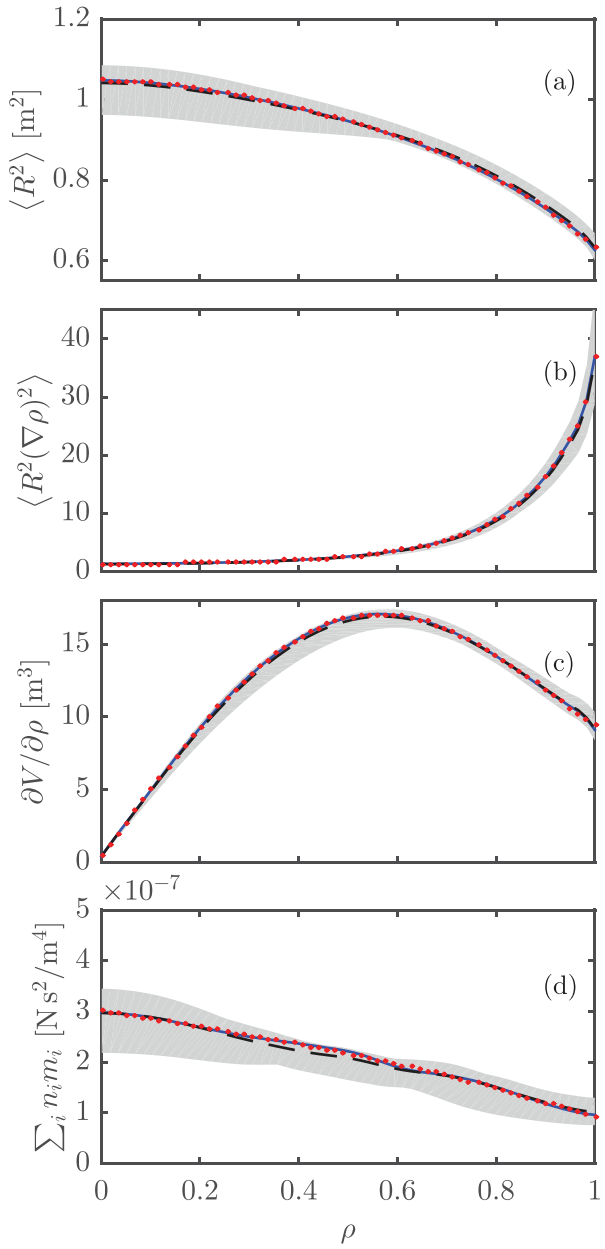

Figure 1. Functions describing the radial profiles of the geometrical properties: $\langle R^2\rangle$, $\langle R^2(\nabla\rho)^2\rangle$, $\partial V/\partial\rho$ and the mass density $\sum_i n_i m_i$ from a TRANSP analysis of plasma discharge 133 367. The shaded region represents the value of the function spanned over time interval (0.45–0.92) s. The time-average values are shown by the black dashed line (– –), the fixed time values and its curve-fit are shown by the solid blue lines (—) and the red dots (o) respectively.

A key parameter in the model is the diffusion coefficient χ_ϕ, which we take to be constant in time in (2). There are no direct measurements of χ_ϕ inside the tokamak, but TRANSP is able to reconstruct a value for χ_ϕ for an experiment where ω is measured. Figure 2 shows the deduced χ_ϕ from a particular run (plasma discharge number 133775). This run is identical to the plasma discharge number 133367 except that it does not have an applied non-axisymmetric field, and therefore $T_{\mathrm{NTV}} = 0$. This feature is very important because each dissipation effect needs to be considered separately from each source in the model. The data driven model will use the χ_ϕ

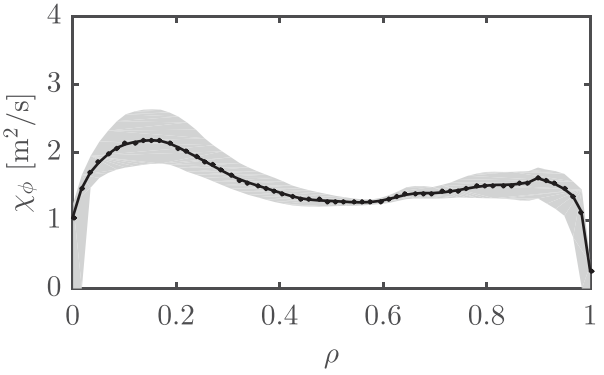

Figure 2. The momentum diffusivity coefficient χ_ϕ is calculated through TRANSP analysis of plasma discharge 133775. The shaded region represents the value of the function spanned over time interval (0.45–0.92) s. The time-average values and its curve-fit are shown by the circles and the solid line respectively.

of discharge (133775) as its momentum diffusivity coefficient reference.

The approach here is as follows: given a range of desired profiles that the operator wishes the system to reach and stabilize, take the simplified model (2) that relies on different models of n m, NTV and NBI torques from a representative class of plasma discharge (χ_ϕ modeled from plasma discharge 133775), linearize the model around an equilibrium whose basin of attraction contains the range of desired profiles and use the linearized model to design a controller that will attempt to match any target shape within this range.

2.2. Actuator models

In order to control the toroidal momentum of the plasma in a spherical tokamak, we consider the use of two actuator mechanisms, namely, the neutral beam injection (NBI) and the neoclassical toroidal viscosity (NTV). The neutral beams are the main sources of momentum for the plasma and the NTV actuator is primarily used as a source of drag on the plasma. For NSTX, T_{NBI} is strongest in the plasma core, whereas T_{NTV} is strongest closer to the edge of the plasma. The momentum diffusivity χ_ϕ allows transport of the momentum across these plasma regions on the momentum diffusion timescale of about 0.1 s in NSTX H-mode plasmas.

2.2.1. Neutral beam injection (NBI). In NSTX, neutral beam injection is the main method to produce positive torque to increase plasma rotation, which is achieved by injecting high-speed neutral atoms into the center of the plasma. Neutral atoms are able to cross the confining magnetic field of the tokamak without being deflected, and are ionized in the plasma via collisions with ions and electrons. The fast ions that are generated are also confined in the magnetic field and are able to exchange their energy to plasma ions and electrons. Typical injection acceleration voltages are in the range of 50 keV to 130 keV and for comparison, in NSTX, the peak plasma ion thermal temperature reaches up to 1.5 keV. Figure 3 shows the planned neutral beam injection for the present upgrade of NSTX. In the present study, we consider the three

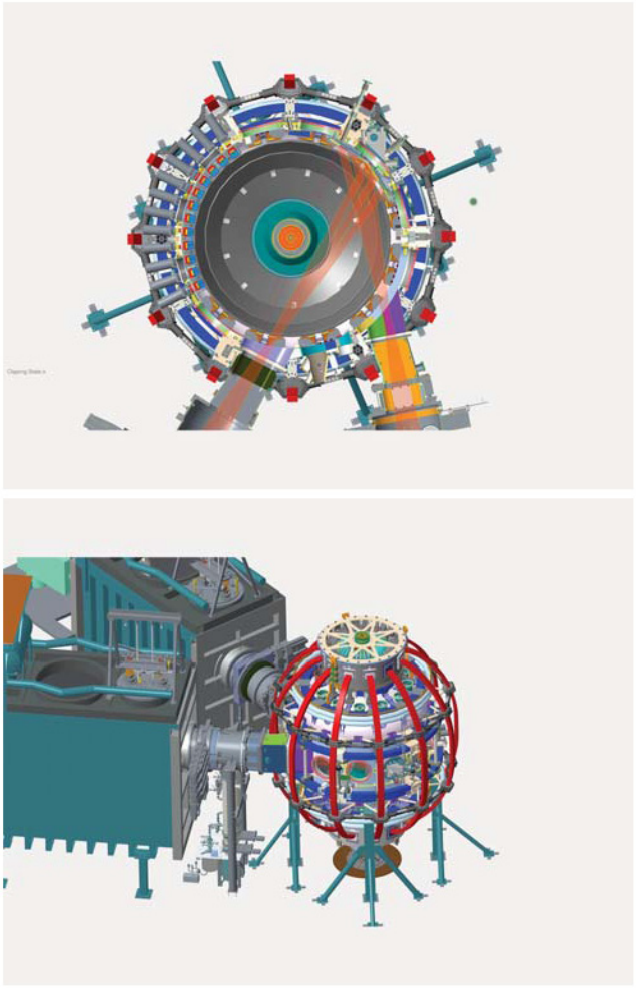

Figure 3. Illustration of the neutral beam injection (NBI) devices for NSTX-U with an inside view from the top of the tokamak (top) and outside view (bottom).

neutral beam sources injected from the injector shown on the left of the figure. Furthermore, for simplicity, we model the three sources as a single torque input, as we describe below.

A differential-equation model is introduced to relate the input power to the generated torque. First, we approximate the NBI torque as a product of the spatial average of the torque, $\overline{T}_{\mathrm{NBI}}(t) \equiv \mathrm{avg}_\rho T_{\mathrm{NBI}}(t,\rho)$, and a function, $F_{\mathrm{NBI}}(\rho)$, that represents the spatial profile

$$T_{\mathrm{NBI}}(t,\rho) = \overline{T}_{\mathrm{NBI}}(t) F_{\mathrm{NBI}}(\rho), \tag{4}$$

where the spatial profile of the torque is taken to be a Gaussian function (based on TRANSP analysis of NSTX discharge 133367) written as

$$F_{\mathrm{NBI}}(\rho) = a_{\mathrm{NBI}} \exp\left(-\frac{\rho^2}{2\sigma_{\mathrm{NBI}}^2}\right). \tag{5}$$

Figure 4(a) shows the deduced profile F_{NBI} of the torque generated by the neutral beams, where the parameters $a_{\mathrm{NBI}} = 7.9090$ and $\sigma_{\mathrm{NBI}} = 0.2219$ were determined by a least-squares fit to the time-averaged data.

In our model, the spatial average of the torque $\overline{T}_{\mathrm{NBI}}(t)$ is related to the power input, $P_{\mathrm{NBI}}(t)$, by a first-order lag:

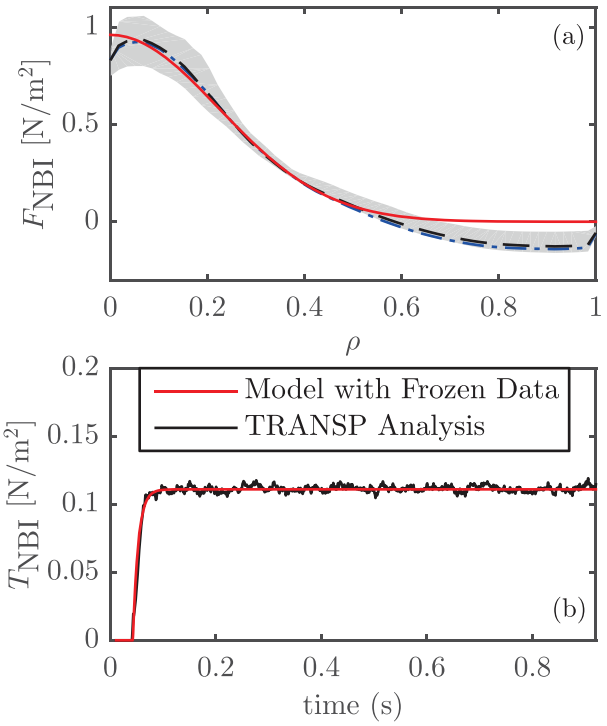

Figure 4. (*a*) Spatial profile for the neutral beam torque (F_{NBI}) for plasma discharge 133367. The shaded region represents the values for times ranging from 0.45 to 0.92 s: time averaged values (– –); values at the fixed time $t = 0.6$ s (– ·); and the fit (5) (—). (*b*) Spatial average of the torque generated for the same plasma discharge ($\overline{T}_{\mathrm{NBI}}$), showing the TRANSP analysis (black) and the model (6) (red), with $\tau_{\mathrm{NBI}} = 0.01$ s and $\kappa_{\mathrm{NBI}} = 2 \times 10^{-6}$.

$$\frac{\partial \overline{T}_{\mathrm{NBI}}}{\partial t} + \frac{\overline{T}_{\mathrm{NBI}}}{\tau_{\mathrm{NBI}}} = \kappa_{\mathrm{NBI}} P_{\mathrm{NBI}}(t), \tag{6}$$

where τ_{NBI} is the approximate slowing down time of the fast neutral beam particles to impart energy to the bulk plasma and κ_{NBI} is a scalar used to normalize the neutral beam power P_{NBI}. τ_{NBI} depends on the collisionality and can affect the response time of the beam power actuator. For values of τ_{NBI} between 10 and 30 ms, the impact that the actuator has on the control does not change significantly. By fitting equation (6) with TRANSP analysis of figure 4(*b*), τ_{NBI} is set to 0.01 s.

Figure 4(*b*) shows the solution of equation (6) with P_{NBI} fixed to 6 MW, compared with the neutral beam torque predicted by TRANSP analysis, which uses a more elaborate Monte Carlo model.

2.2.2. Neoclassical toroidal viscosity (NTV). Tokamaks usually have error fields or magnetohydrodynamic (MHD) activities present and these imperfections break the toroidal symmetry of the magnetic field and result in enhanced neoclassical toroidal plasma viscosity which then increases the rate of toroidal flow damping. The result will be a change of the edge rotation and shear.

For the current one-dimensional toroidal momentum model, we aim to model the momentum loss due to the neoclassical toroidal viscosity in the toroidal average sense and base our model on the work done in [36] from which we can

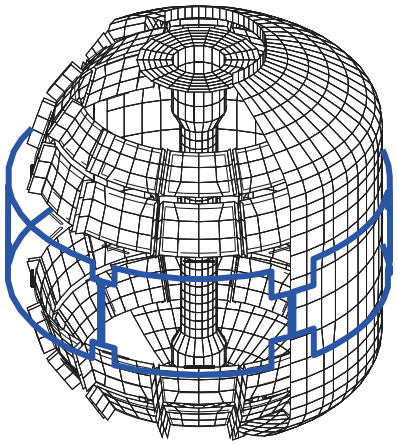

Figure 5. Model representation of the three-dimensional coils (highlighted in blue) used to create the magnetic field that produces NTV in the NSTX device.

design the NTV torque as the bilinear product of the coil (figure 5) current squared (I^2) with the toroidal momentum ω as follows

$$T_{\mathrm{NTV}}(t, \rho) = -K\, G(\rho)\, \langle R^2 \rangle\, I^2(t)\, \omega(t, \rho), \tag{7}$$

where K is a constant and G is a Gaussian function.

The present model will focus on the torque generated by the $n = 3$ applied field 'configuration', in which the current reverses direction in each of the six neighboring coils. Other applied field configurations are possible (e.g. configurations with dominant $n = 2$ component) and have experimentally produced effective NTV as well [4].

The approach in our model is to approximate the general shape of T_{NTV}/ω by a time-invariant spatial profile and a time-evolution of a scalar current, similar to the way T_{NBI} was treated. The resulting model has the form

$$\frac{T_{\mathrm{NTV}}(t, \rho)}{\omega(t, \rho)} = -G_{\mathrm{NTV}}(\rho)\, I^2(t), \tag{8}$$

where

$$G_{\mathrm{NTV}}(\rho) = K\, \langle R^2 \rangle\, G(\rho), \tag{9}$$

and $G(\rho)$ is a Gaussian function centered towards the edge ($\mu = 0.7, \sigma = 0.1$). Figure 6 shows the current that flows into the coils for the plasma discharge 133367. We notice that the current is kept constant after 0.6 s. It should be noted that for control design, the actuator input will be $I^2(t)$. Using the experimental rotation profile, the modeled NTV torque is shown in figure 7.

2.3. Testing and comparing the model

2.3.1. Discretization of the model. In order to numerically simulate the partial differential equation (2), we use a spectral method, projecting onto suitably chosen basis functions, to obtain a system of ordinary differential equations. In particular, we write

$$\omega(\rho, t) = \sum_{n=1}^{N} a_n(t) \varphi_n(\rho), \tag{10}$$

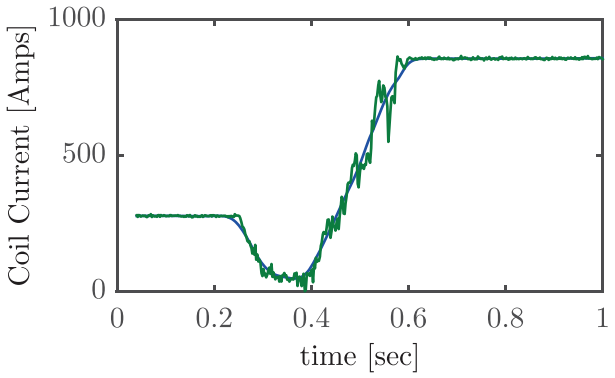

Figure 6. Coil current $I(t)$ for plasma discharges 133367: the green line represents the model from CHERS data and blue lines represent the smoothed data.

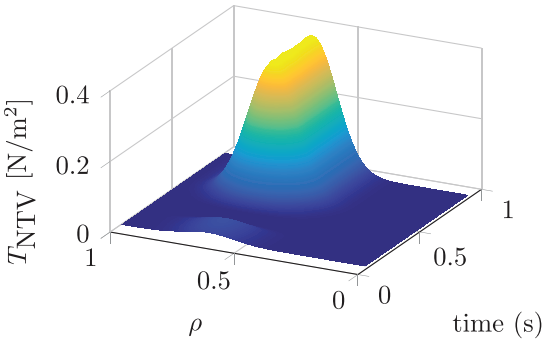

Figure 7. 3D representation of the NTV torque model (7) where ω is taken from experimental measurements of 'fixed' plasma discharge 133367, and I^2 is as shown in figure 6.

where the basis functions are given by

$$\varphi_n(\rho) = J_0(k_n\rho), \qquad n = 1, \ldots, N, \tag{11}$$

where J_0 denotes the Bessel function of the first kind and k_n denotes the n-th root of J_0. With this choice of basis functions, the expansion (10) automatically satisfies the boundary conditions (3), both at $\rho = 0$ (since $J_0'(0) = 0$) and at $\rho = 1$ (since $J_0(k_n) = 0$). Furthermore, the basis functions satisfy the orthogonality relation

$$\langle \varphi_n, \varphi_m \rangle = 0, \qquad \text{for} m \neq n, \tag{12}$$

where the inner product is defined by

$$\langle f, g \rangle = \int_0^1 \rho f(\rho)\, g(\rho)\, \mathrm{d}\rho.$$

Note that 2 is linear in ω, and can be written as

$$\partial\omega/\partial t = L(\omega, T_{NBI}, T_{NTV}), \tag{13}$$

where L is a differential operator linear in each argument. Inserting the expansion (10) into (13), taking inner products with φ_m, and using the orthogonality relation (12) then gives

$$\dot{a}_m = \sum_{n=1}^{N} \frac{\langle L(\varphi_n, T_{NBI}, T_{NTV}(\varphi_n)), \varphi_m \rangle}{\langle \varphi_m, \varphi_m \rangle}, \quad m = 1, \ldots, N,$$

which is a set of N coupled ordinary differential equations for the coefficients a_m.

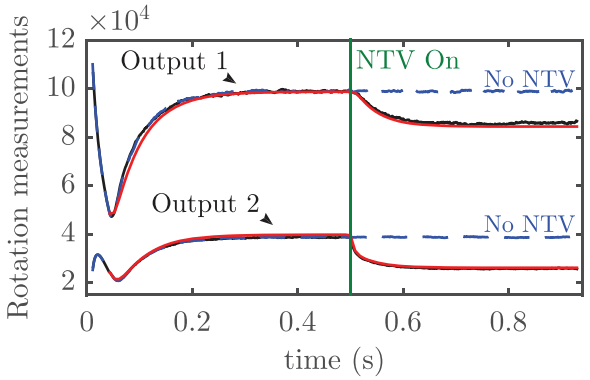

Figure 8. Two rotation measurements with NBI and NTV actuators activated at $t = 0$ s and $t = 0.5$ s respectively, comparing TRANSP analysis with fixed background (black), with the model 2, with $N = 4$ Bessel functions (red).

2.3.2. Comparison model versus TRANSP. The parameters in the model (2) are determined from TRANSP analysis of plasma discharge 133367, as described in section 2. Figure 8 shows the comparison of the model with the TRANSP analysis (prediction of plasma discharge 133367), showing the rotation at two values, $\rho = 0.1346$ and 0.5498. Given two points of measurements of rotation (outputs), one near the core, the other one towards the edge of the tokamak (more details in the next section); the model and TRANSP are first run with only the NBI actuator on (6 MW), then at $t = 0.5$ s, the NTV actuator is turned on for both models with the same value.

Figure 8 shows these rotation measurements for the simplified model (red) compared against TRANSP analysis (solid black line) when the NBI and NTV actuators are activated at $t = 0$ s and $t = 0.5$ s respectively. The blue dashed line shows the steady values reached when only NBI is activated. It shows that the model is a good approximation of the TRANSP analysis model.

Figure 9 shows how the simplified model performs for a different plasma discharge (133743), at conditions different from those for which the model was calibrated. Projecting the simplified model onto 40 Bessel modes yields little improvement over using only 4 modes so we use $N = 4$ modes for the rest of the modeling. The relative error between the reduced model and experimental data (which is the difference between the experimental and the model rotation divided by the mean of the spatial average of the experimental rotation data) is also shown in the same figure.

For all the models, the initial condition is set to be the experimental rotational frequency at time $t = 0.4$ s after the start up ($t = 0$) and when the plasma reaches the H-mode.

An exact plasma model is not a major concern as feedback control can be performed to tolerate errors in the model. The key is to ensure the model does not deviate drastically from the actual profile in order to prevent control system instabilities from dominating plasma physics dynamics.

This simplified model (derived plasma discharge 133367) has been extensively validated against other plasma discharges in NSTX analysis (showing here 133743). The error remains acceptable starting with less than 25% for the experimental data 133743 where the original model was maintained

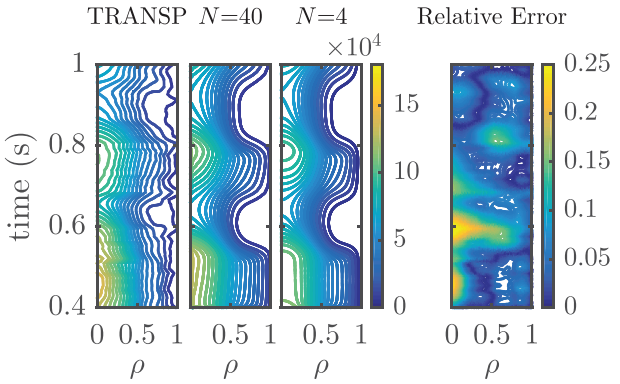

Figure 9. Comparison of the rotational frequency ω for plasma discharge 133743, comparing TRANSP analysis (left), with the simplified model (2), projected onto $N = 40$ Bessel modes, and $N = 4$ Bessel modes. Also shown is the relative error between TRANSP and the reduced model ($N = 4$).

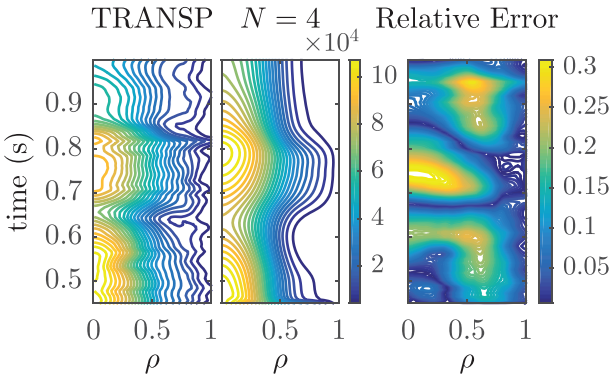

Figure 10. Comparison of the rotational frequency ω for plasma discharge 133751, comparing TRANSP analysis (left), with the simplified model (2), projected onto $N = 4$ Bessel modes. Also shown is the relative error between TRANSP and the reduced model ($N = 4$).

the same, only the density and the input torques were updated. Figure 10 shows how the simplified model performs for another different plasma discharge (133751). The error does not exceed 30% for other experimental comparisons.

The overall behavior of the plasma is captured qualitatively very well using the simplified model of equation (2) with a fixed background.

3. Linear plasma rotation control

The purpose of this section is to demonstrate that standard model-based control techniques may be used to guide an experimental plasma rotation profile to track a desired reference. Some approaches on how controllers can be designed to achieve a desired profile with a reasonable response time are presented in the following sections.

Recall that the two actuators available to the controller are the (NBI) beam power and the coil current producing NTV. In this case, a state-space realization is derived and linear quadratic regulators are used to design a feedback controller that is optimal in minimizing a prescribed quadratic cost function.

3.1. State space realization

In order to be able to use linear control tools, a state-space realization of equation (2) shifted around a steady state has to be built. Let $\bar{\omega}$ be the steady state reached for the given beam power $\bar{P}$ and coil current $\bar{I}$. The linearization around this steady state profile can be written as

$$\omega(t,\rho) = \bar{\omega}(\rho) + \omega'(t,\rho), \tag{14}$$

$$I(t) = \bar{I} + I'(t), \tag{15}$$

$$P_{\mathrm{NBI}}(t) = \bar{P} + P'(t), \tag{16}$$

where ω', I' and P' are the respective perturbations to the equilibria $\bar{\omega}$, $\bar{I}$ and $\bar{P}$. By plugging in these equations into equations (2) and (6) and by linearizing equation (7) and simplifying, we obtain

$$\frac{\partial}{\partial t}\begin{pmatrix}\omega'\\ \overline{T}_{\mathrm{NBI}}\end{pmatrix} = \begin{pmatrix}a_{11} & a_{12}\\ 0 & a_{22}\end{pmatrix}\begin{pmatrix}\omega'\\ \overline{T}_{\mathrm{NBI}}\end{pmatrix} + \begin{pmatrix}b_{11} & 0\\ 0 & b_{22}\end{pmatrix}\begin{pmatrix}I'^2\\ P'\end{pmatrix} \tag{17}$$

where

$$a_{11} = \frac{1}{nm\langle R^2\rangle}\left[\left(\frac{\partial V}{\partial\rho}\right)^{-1}\frac{\partial}{\partial\rho}\left(\frac{\partial V}{\partial\rho}(nm)\chi_\phi\langle R^2(\nabla\rho)^2\rangle\frac{\partial}{\partial\rho}\right) - KG(\rho)\langle R^2\rangle I_0^2\right] a_{12} = \frac{F_{\mathrm{NBI}}(\rho)}{nm\langle R^2\rangle}a_{22} = -\frac{1}{\tau_{\mathrm{NBI}}}b_{11} = -\frac{1}{nm\langle R^2\rangle}KG(\rho)\langle R^2\rangle\omega_0 b_{22} = \kappa_{\mathrm{NBI}}$$

Let $x = (a_0, a_1, ..., a_r,\ \overline{T}_{\mathrm{NBI}}(t))$ be the $(r+1)$ Bessel coefficients of the projection of the partial state ω on the r chosen Bessel functions, let $u = (I'^2,\ P') \in \mathbb{R}^p$ be the perturbed input, and $y \in \mathbb{R}^q$ be the perturbed output (sensor measurements from their equilibrium values). This system of equations can be represented in the standard state-space form:

$$\dot{x} = Ax + Bu, \tag{18}$$

$$y = Cx, \tag{19}$$

by using the spectral decomposition described in section 2.3. $A \in \mathbb{R}^{(r+1)\times(r+1)}$, $B \in \mathbb{R}^{(r+1)\times p}$, and $C \in \mathbb{R}^{q\times(r+1)}$ are respectively called the dynamics, control and sensor matrices. Here, there are two actuators ($p = 2$), one power input for the neutral beams and another one for the coil current producing the NTV. The outputs y correspond to the sensor measurements of the plasma toroidal rotation. Here, two measurements are taken, one near the core and one towards the edge of the plasma ($q = 2$).

3.2. Non-zero target state

Once the state-space realization is obtained, the goal is to force the shape of the plasma rotation profile to reach a target

state x_d such that the sensor output y matches a reference signal y_d. In the final implementation, all one should have to prescribe is y_d (e.g. plasma rotational frequency values at certain locations). The target state x_d and the corresponding input u_d are found by solving equations (18) and (19) at steady state ($\dot{x} = 0 = Ax_d + Bu_d$ and $y_d = Cx_d$). We then solve for x_d and u_d by writing in matrix form

$$\begin{pmatrix} x_d \\ u_d \end{pmatrix} = \begin{pmatrix} A & B \\ C & 0 \end{pmatrix}^{-1} \begin{pmatrix} 0 \\ I \end{pmatrix} y_d = \begin{pmatrix} F_x \\ F_u \end{pmatrix} y_d. \tag{20}$$

Note that for this case, there is always a unique solution, since the number of inputs equals the number of outputs ($p = q = 2$), A is invertible, and there are no transmission zeros at steady state.

3.3. Control design

Once the target states (x_d, u_d) are established, the controllers are designed based on the reduced model dynamics, then applied to the full-dimensional linearized model, and finally tested on the original nonlinear model to determine if the controller can suppress disturbances and reach the desired profile in the vicinity of the equilibrium.

3.3.1. Full-state feedback control design. When the reduced-order model (in Bessel basis) is obtained, a feedback control law can be constructed as

$$u = u_d - K(x - x_d) = -Kx + Fy_d, \tag{21}$$

where K is the feedback control gain to be determined from control design and $F = F_u + KF_x$ is the feedforward gain. Therefore, the resulting closed-loop system can be written as

$$\begin{aligned} \dot{x} &= (A - BK)x + BFy_d, \\ y &= Cx. \end{aligned} \tag{22}$$

In order to design the controller from equation (21), we have to choose the gains K. A standard linear control technique (linear-quadratic regulators) is used in order to determine those gains while minimizing a quadratic cost function of the form:

$$\mathcal{J} = \int_{t_0}^{\infty} (x^T Q x + u^T R u) \mathrm{d}t, \tag{23}$$

where $Q \geqslant 0$ and $R > 0$ are symmetric matrices chosen by the control designer. Q will be chosen to be equal to $q\, C^T C$ where q is a constant and R is a 2×2 diagonal matrix, which reduces equation (23) to

$$\mathcal{J} = \int_{t_0}^{\infty} (q\, y^T y + u^T R u) \mathrm{d}t. \tag{24}$$

The input u, from equation (21), that minimizes $\mathcal{J}$ is obtained by setting

$$K = -R^{-1} B^T P, \tag{25}$$

where P is a positive-definite, symmetric matrix that solves the algebraic Riccati equation: $PA + A^T P - PBR^{-1}B^T P + Q = 0$. This equation is solved numerically using standard routines in MATLAB. For more details about the method, see standard references such as [45, 46]. It should be noted that the feedforward gain F depends on the matrices A, B, C and K.

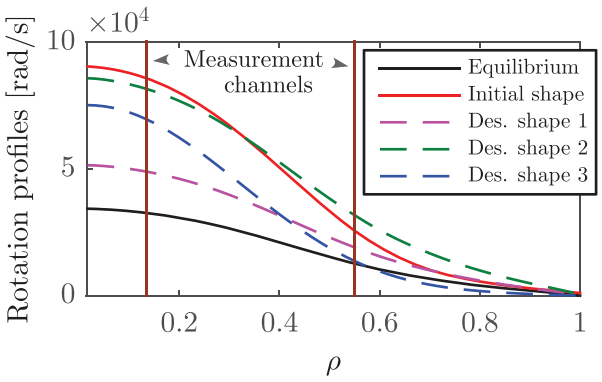

Figure 11. Rotation profiles: definition of the initial profile, equilibrium profile w_0 used for the linearization and the desired profiles to reach w_d. The measurement points r are the intersections of the different profiles with the measurement channels

Figure 11 defines our initial profile, the equilibrium profile used for the linearization and the targeted profile where the measurements are done. In this paper we use $q = 10^4$ and $R = I$ by inspection of the magnitude of our inputs and outputs.

3.3.2. Observer-based feedback control design. The feedback law (21) we designed in the previous section requires knowledge of the full state x. However, in an actual experiment, we cannot measure the state directly; we measure only the outputs y. However, we may reconstruct an estimate of the state from the available sensor measurements using an *observer*. A standard linear observer reconstructs a state estimate $\hat{x}$, with dynamics given by

$$\begin{aligned} \dot{\hat{x}} &= A\hat{x} + Bu + L(y - C\hat{x}) \\ &= (A - LC)\hat{x} + Bu + Ly, \end{aligned} \tag{26}$$

where the matrices A, B and C are the same as those in the model (22), and L is a matrix of gains chosen such that the state estimate converges quickly relative to the system's dynamics. Using our linear model, we design an optimal observer (Kalman filter) to find L. We introduce two zero-mean Gaussian white noise processes, w the process disturbance and v the sensor noise, with respective covariance matrices W and V, into equations (18) and (19) to obtain

$$\dot{x} = Ax + Bu + w, \tag{27}$$

$$y = Cx + v. \tag{28}$$

Then the covariance of the error in the state estimate is minimized (assuming the noise models are correct) by setting

$$L = PC^T V^{-1}, \tag{29}$$

where P is a positive-definite, symmetric matrix that solves the algebraic Riccati equation: $AP + PA^T - PC^T V^{-1} CP + W = 0$. This equation is solved numerically using standard routines in MATLAB. For more details about the method, see standard references such as [45, 46]. In this paper, we use $W = \mathrm{diag}(10^4 I_r, 0)$

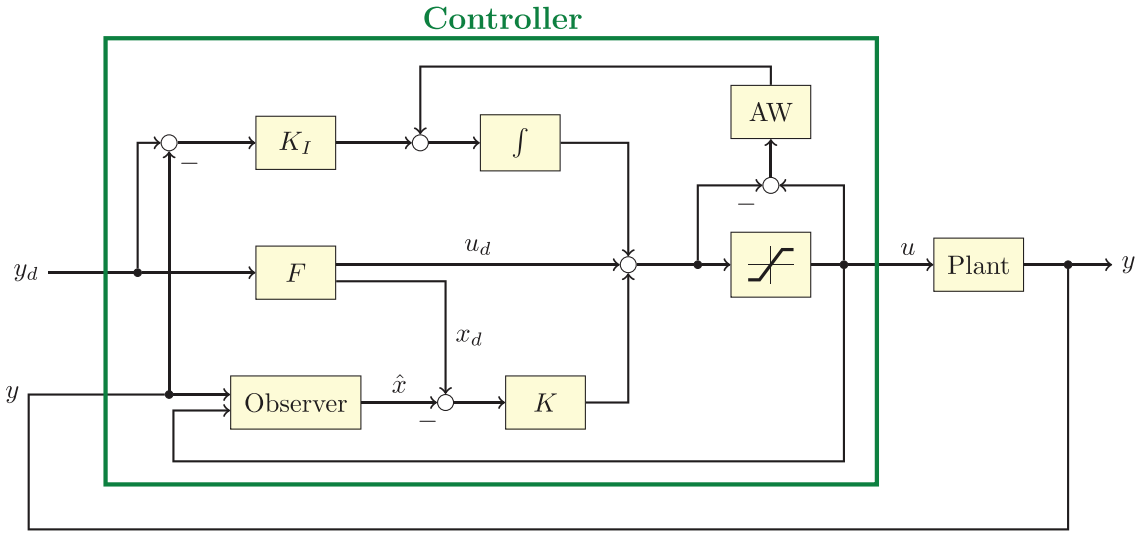

Figure 12. Global schematic of the controller that combine a feedforward (F), a LQR (K), an observer, an integrator (K_I) and an anti-windup (AW).

and $V = I$. The observer generates an estimate of the state from the physics model as represented by the state matrix, the inputs and outputs, and once combined to the feedback controller it forms a linear quadratic Gaussian compensator.

3.3.3. Integrator, actuators saturation and anti-windup design. Because the primary goal is tracking the desired rotation profile, we want to minimize the steady state error between the output (measured) and the target profile. One way to handle such issue is to use integral action, introducing a new state variable z that is the integral of the error:

$$\dot{z} = y_d - y = y_d - Cx. \tag{30}$$

The overall system can be then written as

$$\frac{\partial}{\partial t}\begin{pmatrix} x \\ z \end{pmatrix} = \begin{pmatrix} A & 0 \\ -C & 0 \end{pmatrix}\begin{pmatrix} x \\ z \end{pmatrix} + \begin{pmatrix} B \\ 0 \end{pmatrix}u + \begin{pmatrix} 0 \\ I \end{pmatrix}y_d \tag{31}$$

with a new feedback law designed as

$$u = \begin{pmatrix} -K & K_I \end{pmatrix}\begin{pmatrix} x \\ z \end{pmatrix} + Fy_d = u_d + K(x_d - x) + K_I\int(y_d - y) \tag{32}$$

where the gains K and K_I can be determined through the MATLAB command LQI which solves an algebraic Riccati equation with an extended state that includes the integrator. A drawback of integral control is that if the actuator values are limited to some range $u \in [u_{\min}, u_{\max}]$ (as they are in our case), then the integrator can accumulate error when the actuator is 'saturated', resulting in poor transient performance, a phenomenon known as 'integrator windup'. We avoid these effects by using a standard anti-windup scheme (see, e.g. [46, 47]), in which one feeds back the difference between the desired value of u and its actual (possibly saturated) value, as shown in the diagram in figure 12.

Figure 12 shows the schematic of the overall controller, combining the feedback law (21) with the observer (26), the integrator (30) and the anti-windup approach described above.

4. Simulation results

The goal of the simulations is to test the controller first on the simplified reduced-order model, and then on a higher fidelity model (TRANSP) that is closer to the actual experiment. The desired profiles shown in figure 11 will be targeted in both cases and the results will be compared to see the effectiveness of the controller described above.

4.1. Actuator constraints

Both actuators (NTV coil current and NBI beam power) have constraints that need to be satisfied when applied on the real device (NSTX). Some of these constraints are made for the safety of the operations, some of them reflect the practicability and the feasibility of some requests to the device. The constraints will be added to the dynamics equations.

The coil current will be constrained between 0 and 3000 amperes. The coil current response is fast compared to the dynamics of the system that it can be assumed to be applied instantaneously.

Although we have so far been treating the NBI actuator as a single source outputting between 2 and 6 MW of power, it is actually composed of 3 beams. Each beam can either be on and produce 2 MW of power or off and produce 0 MW. In addition, each beam can only be switched on or off a maximum of 20 times per plasma discharge to prevent device fatigue issues, and there is a refractory period of 10 ms after each switch during which the beam cannot be switched again. Due to diagnostic considerations, one NBI source is typically always on, and so the overall injected power is considered to be between 2 and 6 MW here.

These physical restrictions constrain the model and controller to be discrete and to use Pulse Width Modulation (PWM) for the beam power actuation in order to obtain control requested values between 2 and 6 MW.

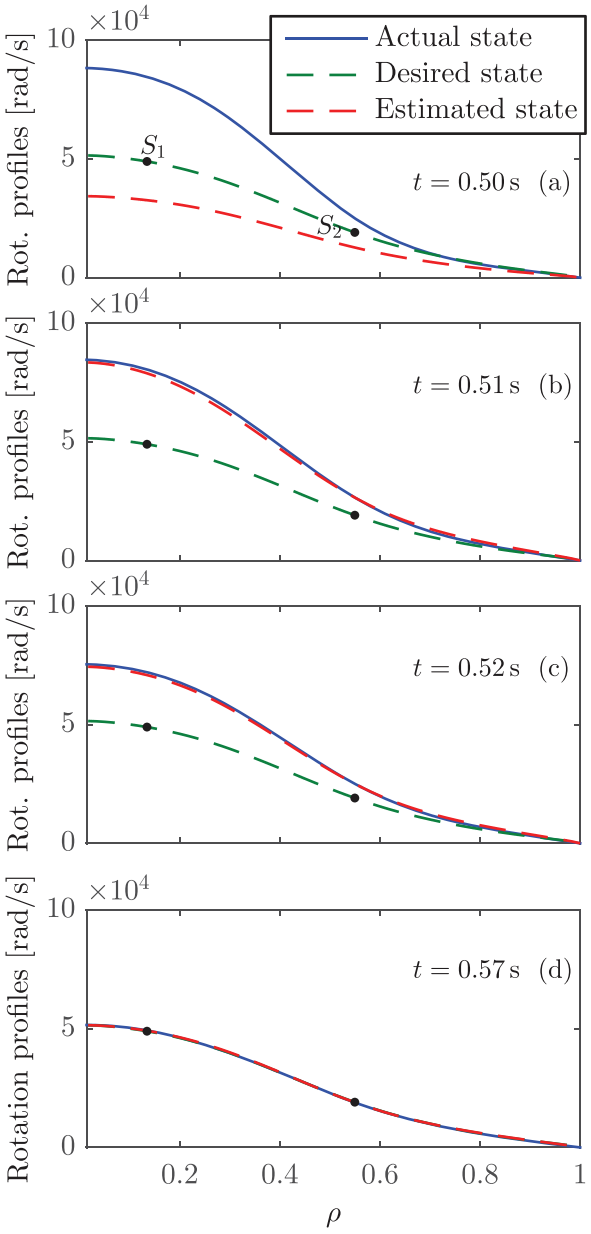

Figure 13. Time evolution of the rotation in the model as it evolves toward the target values and its estimate at 4 different times. The green profile is the targeted rotation profile. The red profile is the estimated state. The blue profile is the actual state. Points S_1 and S_2 indicate the locations of the sensors.

4.2. Simulation without PWM

The discretized controller is first applied to the reduced-order model, considering only the constraint of saturation for both actuators. It is thus considered that any values of beam power between 2 and 6 MW and coil current between 0 and 3000 Amps can be applied instantaneously.

Figure 13 shows the rotation profile, comparing the actual profile, the desired profile, and the profile estimated by the observer. Four different times are shown: 0.5 s (at which time the controller is turned on), 0.51 s, 0.52 s and 0.57 s respectively. The two sensors locations are indicated in the figure, and it can be noticed that the targeted profile is reached in less than 0.1 s.

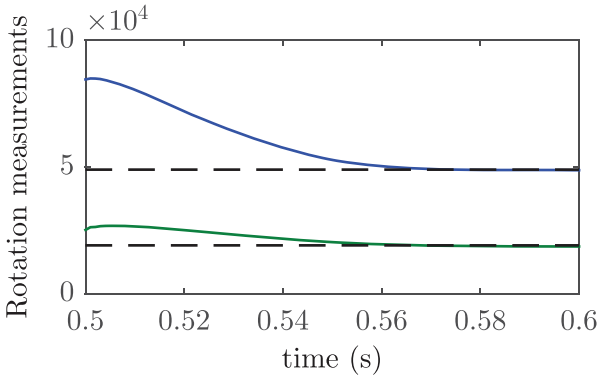

Figure 14. Time evolution of the rotation measurement at the two sensor points. The dashed lines represents the desired measurements at these latter locations.

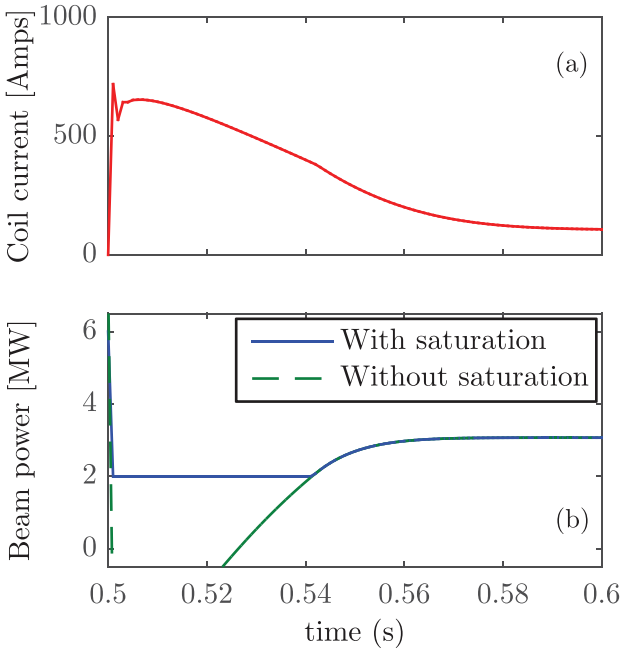

Figure 15. Time evolution of the coil current and the overall beam power and its saturation, needed to reach the 1st desired profile

Figure 14 shows the time evolution of the rotation measurement focused at the two sensor points located at the core and towards the edge of the plasma only. The outputs track the desired values well after about 50 ms.

Figure 15 represents the requested inputs (coil current and overall beam power) needed to reach the desired profile of figures 13 and 14. It can be noticed that the current does not saturate whereas the beam power does.

Because the initial profile (figure 13(*a*)) before turning the controller on, is above the targeted profile (figure 13(*d*)), and the difference between the two profiles is higher towards the core of the plasma (where the beam power acts), the controller tries to first push the power down starting from 6 MW at the initial state before controlling, up to 2 MW when it hits saturation. The green dashed line in figure 15 shows how the controller would apply the beam power if no saturation was in effect. During the rapid decrease of the beam power, the controller increases the coil current in order to increase the drag

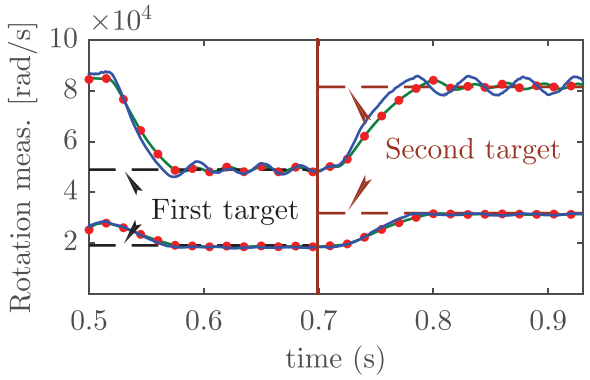

Figure 16. Comparison of the rotation measurements when PWM is applied for both the reduced-order model (green lines) and the TRANSP predictive model (blue lines). The red dots represents the cycle times (every 0.015 s).

and forces rapid deceleration towards the edge of the plasma. The controller and the actuators, when they can be activated instantaneously, enable the rotation profile to reach its target about 2 times faster (about 60 ms) than the momentum diffusion time (about 100 ms).

4.3. Computational approach for TRANSP

In order to predict the toroidal rotation for NSTX, the TRANSP code running in predictive mode is used for a given beam power and coil current. It also takes as inputs the time histories of the plasma boundary shape, plasma current, electron and ion (Chang–Hinton model [48]) temperature and density profiles and the momentum diffusivity coefficient.

The actuator commands needed for closed-loop rotation control simulations are entered into the TRANSP code, which serves as a plasma simulator for testing the present controller. For more details on the TRANSP implementation, see [49].

4.4. Simulation with PWM

The discretized controller is now applied to the reduced-order model and the TRANSP predictive model, considering all the constraints listed in section 4.1 for both actuators. The main difference with section 4.2 will be that instead of applying the exact beam power numerical value as requested by the controller, each of the 3 beams will be modulated individually while satisfying all the constraints.

At the beginning of each duty cycle, the controller sets the requested power. During the duty cycle, the beams switch on and off at most once to minimize the number of switches. Because of this and the 10 ms refractory period, the exact requested power cannot always be met.

Durations greater and smaller than 10 ms are chosen to compare output results for different duty cycle durations. The longer the duty cycle, the better for the device because it means less commands switches so less fatigue, but a longer duration introduces a longer controller lag which impairs performance.

Figure 16 compares the rotation measurements when the PWM controller is applied to both the reduced-order model

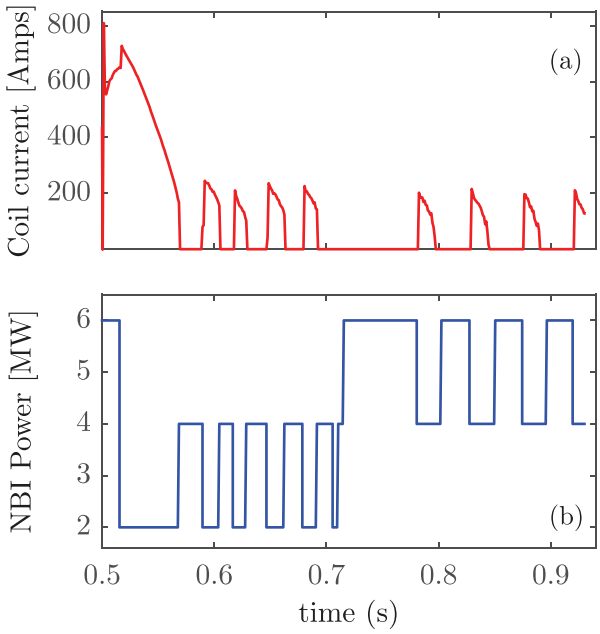

Figure 17. Time evolution of the coil current (a) and the overall beam power (b). The cycle time is 0.015 s.

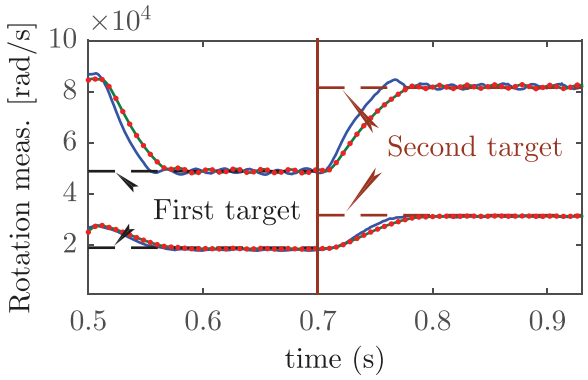

Figure 18. Comparison of the rotation measurements when PWM applied for both the reduced-order model (green lines) and the TRANSP predictive model (blue lines). The red dots represents the cycle times (every 0.006 s).

and the TRANSP predictive model in order to reach two targets, one at $t = 0.5$ s, and the other starting at $t = 0.7$ s. Before $t = 0.5$ s, both models are not controlled (open loop), the measurements are already shown to be the steady-state values shown in figure 8. At $t = 0.5$ s, the controller is turned on (closed loop), and the goal is to reach the first target profile measurement points defined by the two red dots in figure 11. At $t = 0.7$ s, the target profile changes to the second one which is defined by the two blue dots in figure 11. The green line represents the reduced-order model outputs, the blue line represents the TRANSP model. The oscillations are due to the modulations that occurs on each of the beam power source. The total beam power is represented in figure 17(*b*). The coil current in this case (figure 17(*a*)) changes to compensate for when the beam power is too high in order to decrease the toroidal rotation and thus limit the rotation overshoot. In this example, the duty cycle duration is 15 ms which gives a

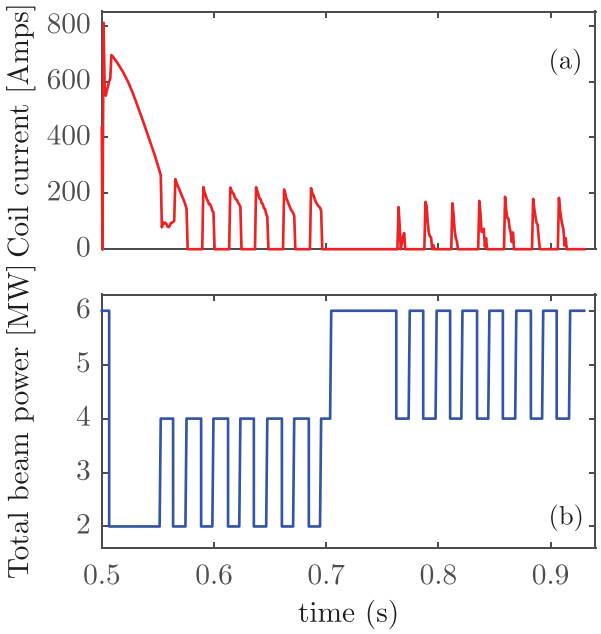

Figure 19. Time evolution of the coil current and the overall beam power (cycle time 0.006 s).

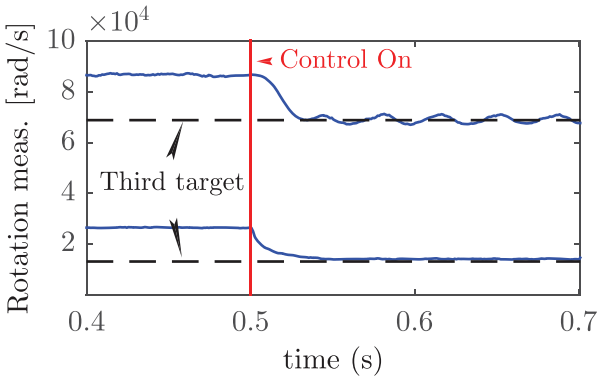

Figure 20. The rotation measurements for the TRANSP predictive model (blue lines). The control is activated at 0.5 s.

reasonable amplitude of oscillation while reaching both targets within the momentum diffusion time (0.1 s).

Figures 18 and 19 represent the same quantities as in figures 16 and 17 respectively, but for a different duty cycle duration (6 ms) which is smaller that the the 10 ms refractory period. The resulting rotation measurements are more oscillatory but the amplitude is better damped. The trade off is that we have to activate the controller more often and thus formulate more requests to the real device.

The reduced-order model in both cases is very close to the TRANSP which again shows that the simplified model gives us a good qualitative approximation of the TRANSP rotation prediction model.

A more peaked profile represented in figure 11 by the third blue desired shape is finally tested. Figure 20 shows the rotation measurements when the PWM controller is applied to the TRANSP predictive model in order to reach this target starting at $t = 0.5$ s. The corresponding total beam power is represented in figure 21(b) and the coil current in figure 21(a). We can see that this case uses a much higher coil current

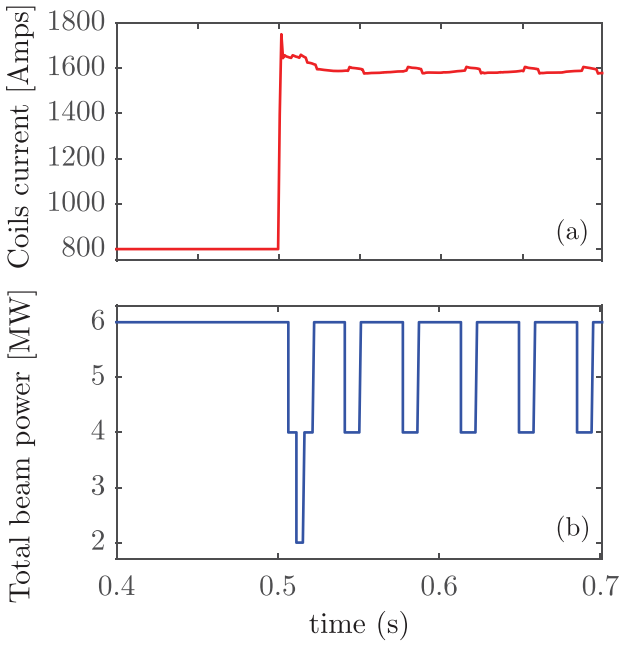

Figure 21. Time evolution of the coil current (a) and the overall beam power (b) for the third target (cycle time 0.006 s).

quantity (about 1.6 kA) in order to push the rotation profile's tail down while keeping the plasma core rotation high.

5. Summary and conclusions

A simple reduced-order model has been developed to capture the rotational toroidal momentum balance for the NSTX device. This model was utilized to control the plasma about its desired profile with the neutral beam injection and the neoclassical toroidal viscosity. The output from the model have been compared with analysis from a predictive model of NSTX and were found to be in good agreement. Based on this simplified model, a complete feedback control design using optimal control techniques as shown above and enables controlling the plasma about a desired profile. This reduced-order controller was then tested using the NSTX predictive model and enabled the rotation profile to reach the desired profile.

Generally, broader toroidal rotation profile brings more stability to the plasma [4] and local rotation shear can affect MHD modes [2]. In the new upgrade of the device, NSTX-U, three additional NBI sources (figure 3) will provide significantly different torque profiles which can affect a broader region of the plasma, specifically towards the edge and can change the shear locally. In this case, the controller can use these added beam sources allowing significantly greater control of plasma instabilities. Furthermore, while only the $n = 3$ applied field configuration was considered for the NTV actuator, it is possible to include different applied field spectra which can change the NTV torque profile. For example, an $n = 1$ field configuration can allow a deeper penetration of this torque profile which will expand the capability of rotation control.

The present controller was designed using models tuned to match experimental data. A next step could be to develop control-oriented models directly from simulations. This

capability would have a large impact: fewer experiments would be needed to calibrate the models/controllers, and more importantly, one could predict actuator requirements (e.g. amplitude, bandwidth, latency), and any inherent performance limitations for future machines such as FNSF. These control-oriented models such as those being developed using TRANSP for NSTX-Upgrade will be tested for their robustness in producing greater range of target profile shapes.

Acknowledgments

This work was supported by the US Department of Energy under contract No. DE-AC02-09CH11466 (PPPL) and US Department of Energy grant number DE-FG02-99ER54524 (Columbia University).

References

[1] Ono M. *et al* and NSTX Team 2000 Exploration of spherical torus physics in the nstx device *Nucl. Fusion* **40** 557
[2] Gerhardt S.P. *et al* 2009 Relationship between onset thresholds, trigger types and rotation shear for the $m/n = 2/1$ neoclassical tearing mode in a high-spherical torus *Nucl. Fusion* **49** 032003
[3] Park Y.S. *et al* 2013 Investigation of mhd instabilities and control in kstar preparing for high beta operation *Nucl. Fusion* **53** 083029
[4] Sabbagh S.A. *et al* 2010 Advances in global mhd mode stabilization research on NSTX *Nucl. Fusion* **50** 025020
[5] Berkery J.W., Sabbagh S.A., Betti R., Hu B., Bell R.E., Gerhardt S.P., Manickam J. and Tritz K. 2010 Resistive wall mode instability at intermediate plasma rotation *Phys. Rev. Lett.* **104** 035003
[6] Biglari H., Diamond P.H. and Terry P.W. 1990 Influence of sheared poloidal rotation on edge turbulence *Phys. Fluids* B **2** 1–4
[7] Terry P.W. 2000 Suppression of turbulence and transport by sheared flow *Rev. Mod. Phys.* **72** 109–65
[8] Hahm T.S. 1994 Rotation shear induced fluctuation decorrelation in a toroidal plasma *Phys. Plasmas* **1** 2940–4
[9] Sabbagh S.A. *et al* 2013 Overview of physics results from the conclusive operation of the national spherical torus experiment *Nucl. Fusion* **53** 104007
[10] Peng Y.K.M. *et al* 2005 *Plasma Phys. Control. Fusion* **47** B263
[11] Peng Y.K.M., Canik J.M. and Diem S.J. 2011 *Fusion Sci. Technol.* **60** 441
[12] Peng Y.K.M. *et al* 2009 *Fusion Sci. Technol.* **56** 957
[13] Schuster E. and Krstic M. 2002 Nonlinear boundary control of non-burning plasma kinetic profiles in cylindrical geometry *Proc. of the 41st IEEE Conf. on Decision and Control* vol 3 pp 2992–7
[14] Boyer M.D. and Schuster E. 2011 Backstepping control of density and energy profiles in a burning tokamak plasma *50th IEEE Conf. Decision and Control and European Control Conf.* pp 1993–8
[15] Schuster E., Krstic M. and Tynan G. 2001 Nonlinear control of burn instability in fusion reactors *Proc. of the 40th IEEE Conf. on Decision and Control* vol 2 pp 1298–303
[16] Schuster E., Krstic M. and Tynan G. 2002 Nonlinear burn control in fusion reactors *19th Symp. on Fusion Engineering* pp 430–3
[17] Schuster E., Krstic M. and Tynan G. 2002 Nonlinear lyapunov-based burn control in fusion reactors *Fusion Eng. Des.* 63–4 569–75
[18] Vitela J.E. and Martinell J.J. 1998 Stabilization of burn conditions in a thermonuclear reactor using artificial neural networks *Plasma Phys. Control. Fusion* **40** 295
[19] Boyer M.D. and Schuster E. 2014 Nonlinear control and online optimization of the burn condition in iter via heating, isotopic fueling and impurity injection *Plasma Phys. Control. Fusion* **56** 104004
[20] Boyer M.D., Barton J., Schuster E., Luce T.C., Ferron J.R., Walker M.L., Humphreys D.A., Penaflor B.G. and Johnson R.D. 2013 First-principles-driven model-based current profile control for the diii-d tokamak via lqi optimal control. *Plasma Phys. Control. Fusion* **55** 105007
[21] Boyer M.D., Barton J., Schuster E., Walker M.L., Luce T.C., Ferron J.R., Penaflor B.G., Johnson R.D. and Humphreys D.A. 2014 Backstepping control of the toroidal plasma current profile in the diii-d tokamak *IEEE Trans. Control Syst. Technol.* **22** 1725–39
[22] Barton J.E., Boyer M.D., Shi W., Schuster E., Luce T.C., Ferron J.R., Walker M.L., Humphreys D.A., Penaflor B.G. and Johnson R.D. 2012 Toroidal current profile control during low confinement mode plasma discharges in diii-d via first-principles-driven model-based robust control synthesis *Nucl. Fusion* **52** 123018
[23] Ou Y. and Schuster E. 2009 Controllability analysis for current profile control in tokamaks *Proc. of the 48th IEEE Conf. on Decision and Control, Held Jointly with the 28th Chinese Control Conf. (Shanghai, 15–18 Dec 2009)* pp 315–20
[24] Ebrahimi F. and Prager S.C. 2004 Current profile control by alternating current magnetic helicity injection *Phys. Plasmas* **11** 2014–25
[25] Argomedo F.B., Witrant E., Prieur C., Brémond S., Nouailletas R. and Artaud J.-F. 2013 Lyapunov-based distributed control of the safety-factor profile in a tokamak plasma *Nucl. Fusion* **53** 033005
[26] Maljaars E., Felici F., de Baar M.R., van Dongen J., Hogeweij G.M.D., Geelen P.J.M. and Steinbuch M. 2015 Control of the tokamak safety factor profile with time-varying constraints using mpc *Nucl. Fusion* **55** 023001
[27] Kim S.H. and Lister J.B. 2012 A potentially robust plasma profile control approach for iter using real-time estimation of linearized profile response models *Nucl. Fusion* **52** 074002
[28] Welander A.S., Kolemen E., La R.J., Eidietis N.W., Humphreys D.A., Lohr J., Noraky S., Penaflor B.G., Prater R. and Turco F. 2013 Advanced control of neoclassical tearing modes in diii-d with real-time steering of the electron cyclotron current drive *Plasma Phys. Control. Fusion* **55** 124033
[29] Volpe F.A.G., Austin M.E., La Haye R.J., Lohr J., Prater R., Strait E.J. and Welander A.S. 2009 Advanced techniques for neoclassical tearing mode control in diii-da) *Phys. Plasmas* **16** 102502
[30] Sabbagh S.A., Bell R.E., Menard J.E., Gates D.A., Sontag A.C., Bialek J.M., LeBlanc B.P., Levinton F.M., Tritz K. and Yuh H. 2006 Active stabilization of the resistive-wall mode in high-beta, low-rotation plasmas *Phys. Rev. Lett.* **97** 045004
[31] Scoville J.T., Humphreys D.A., Ferron J.R. and Gohil P. 2007 Simultaneous feedback control of plasma rotation and stored energy on the diii-d tokamak *Fusion Eng. Des.* **82** 1045–50 *(Proc. of the 24th Symp. on Fusion Technology)*
[32] Yoshida M., Sakamoto Y., Sueoka M., Kawamata Y., Oyama N., Suzuki T. and Kamada Y. 2009 Real-time measurement and feedback control of ion temperature profile and toroidal rotation using fast {CXRS} system in jt-60u *Fusion Eng. Des.* **84** 2206–13

[33] Shaing K.C. 1988 Neoclassical quasilinear transport theory of fluctuations in toroidal plasmas *Phys. Fluids* **31** 2249–65
[34] Shaing K.C., Sabbagh S.A. and Chu M.S. 2010 An approximate analytic expression for neoclassical toroidal plasma viscosity in tokamaks *Nucl. Fusion* **50** 025022
[35] Shaing K.C., Ida K. and Sabbagh S.A. 2015 Neoclassical plasma viscosity and transport processes in non-axisymmetric tori *Nucl. Fusion* **55** 125001
[36] Zhu W. *et al* 2006 Observation of plasma toroidal-momentum dissipation by neoclassical toroidal viscosity *Phys. Rev. Lett.* **96** 225002
[37] Podest M. and Bell R.E. 2012 A real-time velocity diagnostic for NSTX *Rev. Sci. Instrum.* **83** 033503
[38] Moreau D. *et al* 2013 Integrated magnetic and kinetic control of advanced tokamak plasmas on diii-d based on data-driven models *Nucl. Fusion* **53** 063020
[39] Goldston R.J., McCune D.C., Towner H.H., Davis S.L., Hawryluk R.J. and Schmidt G.L. 1981 New techniques for calculating heat and particle source rates due to neutral beam injection in axisymmetric tokamaks *J. Comput. Phys.* **43** 61–78
[40] Budny R.V. 1994 A standard dt supershot simulation. *Nucl. Fusion* **34** 1247
[41] Goldston J.R. 1986 Topics in confinement analysis of tokamaks with auxiliary heating *Proc. Course Workshop (Varenna, 3–13 September 1986)* vol 1 pp 165–86
[42] Callen J.D., Cole A.J. and Hegna C.C. 2009 Toroidal rotation in tokamak plasmas *Nucl. Fusion* **49** 085021
[43] Solomon W.M., Kaye S.M., Bell R.E., LeBlanc B.P., Menard J.E., Rewoldt G., Wang W., Levinton F.M., Yuh H. and Sabbagh S.A. 2008 Momentum-transport studies in high $e \times b$ shear plasmas in the national spherical torus experiment *Phys. Rev. Lett.* **101** 065004
[44] Kaye S.M., Solomon W., Bell R.E., LeBlanc B.P., Levinton F., Menard J., Rewoldt G., Sabbagh S., Wang W. and Yuh H. 2009 Momentum transport in electron-dominated nstx spherical torus plasmas *Nucl. Fusion* **49** 045010
[45] Skogestad S. and Postlethwaite I. 2005 *Multivariable Feedback Control: Analysis and Design* (New York: Wiley)
[46] Astrom K.J. and Murray R.M. 2008 *Feedback Systems: an Introduction for Scientists and Engineers* (Princeton, NJ: Princeton University Press)
[47] Stevens B.L. and Lewis F.L. 2003 *Aircraft Control and Simulation* (New York: Wiley)
[48] Chang C.S. and Hinton F.L. 1982 Effect of finite aspect ratio on the neoclassical ion thermal conductivity in the banana regime *Phys. Fluids* **25** 1493–4
[49] Boyer M.D., Andre R., Gates D.A., Gerhardt S., Goumiri I.R. and Menard J. 2015 Central safety factor and β_n control on NSTX-u via beam power and plasma boundary shape modification, using transp for closed loop simulations *Nucl. Fusion* **55** 053033